Mathematical Biosciences and Engineering

http://www.aimspress.com/journal/mbe

MBE, 23(11): 3211–3240.
DOI: 10.3934/mbe.2026111
Received: 24 June 2026
Revised: 30 August 2026
Accepted: 20 September 2026
Published: 03 November 2026

Research article

Mathematical model of electrochemical signaling from transmuting DNA origami nanostructures within biosensors

Allison M. Carson[1], **Wes Caldwell**[1,2], **Ryan M. Evans**[1] **and Anthony J. Kearsley**[1,*]

[1] National Institute of Standards and Technology, 100 Bureau Drive, Gaithersburg, Maryland, 20899, USA

[2] Johns Hopkins University, 3400 N. Charles Street, Baltimore, MD 21218, USA

* **Correspondence:** Email: anthony.kearsley@nist.gov.

Abstract: This manuscript presents a mathematical model and a description of a numerical simulation of the electrochemical processes surrounding transmuting DNA origami nanostructures within a capacitance-signaling biosensor. A modified Poisson-Boltzmann equation is employed to predict the electric potential about a single DNA origami nanostructure, represented by variability of permittivity and background charge within the domain. Differential capacitance is used to determine the capacitance signal from model variables. The solution to the model, as well as the capacitance, is numerically approximated using finite differencing. Nonsmooth and smooth nanostructure treatments are motivated and analyzed, suggesting that while the nonsmooth treatment introduces large numerical error and loses an order of accuracy, the difference in capacitance between the two treatments is far less significant, though still apparent. A parameter study informs numerical refinement choices and demonstrates the variability in solution caused by the modification of ions species in solution as well as maximum ion concentrations. Preliminary observations on device sensitivity are also provided, suggesting that nanostructures placed away from the bottom surface of the device can cause a reduction in sensitivity and some nanostructure designs are more advantageous for capacitance signaling.

Keywords: biosensors; DNA origami; mathematical modeling; Poisson-Boltzmann equation; inite difference methods; diagnostic test design

1. Introduction

Biological field-effect transistors (Bio-FETs) are an emerging class of biosensing devices that enable rapid, sensitive, and portable detection of disease biomarkers, challenging conventional laboratory-based assays which are often time-consuming, labor-intensive, and costly. These sensors have shown great potential to transform point-of-care medical diagnostics, food safety, and biotoxin

defense among other applications, that rely on quick, accurate measurements upon which to make significant assessments [1–4].

In a typical healthcare configuration, a patient's sample is introduced into an electrolyte solution within a sensing chamber. A small applied voltage biases a semiconducting channel located at the base of the chamber, thus establishing an electric field across it. The surface of the semiconductor is functionalized with a selective biochemical recognition element, which we will refer to as the *biochemical gate*, that binds the target biomarker (e.g., antibodies, nucleic acids, or aptamers) and consequently modulates the local electric field at the semiconductor–electrolyte interface. This field modulation alters the channel conductance, producing an electrical signal that can be measured and interpreted as a positive diagnostic response.

Variations in device architecture and sensing strategies further expand the versatility of Bio-FET platforms [5–10]. A similar biosensor of interest, showcased in [11], measures the disturbance to the electric field as a change in capacitance over time. In this device, the biochemical gate consists of DNA origami nanostructures, pictured in Figure 1, that transmute, or reconfigure, upon binding an analyte [12]. The authors find a significant amplification in the capacitance signal, thought to be created by DNA's strong negative charge and low permittivity relative to the surrounding salt water. Due to their versitility, DNA origami nanostructures have been applied to many other biosensors. In [13], the authors implement DNA origami nanostructures in a complementary metal-oxide semiconductor (CMOS) device and develop methodology to reduce variation in capacitance measurements. To detect conformal changes within DNA origami nanostructures, [14] uses microwave microfluidic sensors, finding ionic conductivity measurements to be the strongest indicator of changes. Nanoswitches constructed from DNA origami have been shown to be stable structures over long periods of use and in low magnesium solutions for biosensors using electrical actuation of the levers [15, 16]. In [17], the authors also demonstrate the use of DNA origami nanostructures to bind large targets, such as viruses and large proteins that range from tens to hundreds of nanometers, in an electrochemical biosensor.

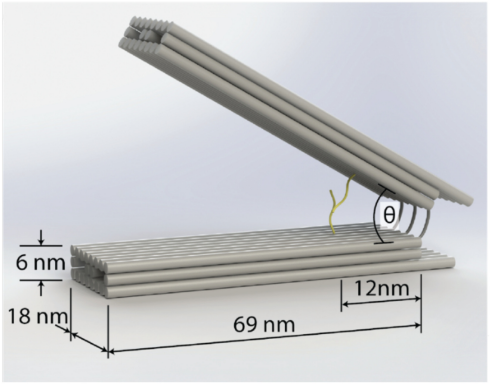


Figure 1. An artistic rendition of a contorting DNA origami nanostructure. Each gray rod represents a double strand of DNA, with two yellow connected strands representing aptamers that limit how wide the nanostructure's upper arm may open. The analyte of interest, if present within the patient's sample, would replace the binding of one of the aptamers, untethering the two such that the upper arm is able to open to a wider angle. The displacement of the DNA alters the established electric field, thus causing device signaling.

Various mathematical models have been put forth to provide deeper insight into biosensor mechanics and to suggest improvement in BioFET designs [18–21]. In studying the design of the biosensor from [11], [22] develops a singular integrodifferential equation that models the concentration of bound ligands at the bottom surface to quantify system parameters such as diffusion coefficients and kinetic rate constants. Despite a singularity, the authors develop a numerical approximation of the solution that converges at an order-of-accuracy of three-halves in time and two in space. System parameters were estimated by minimizing an output-least-squares function and were found to bring excellent agreement with experiment. In [23], a statistical regression method was applied to the device capacitance time series to separate noise from signal, thus facilitating qualitative data analysis of device measurements. Additionally, the authors suggest an optimal bandwidth parameter to determine coefficients, which was found to remain consistent across various device chamber aspect ratios.

In this manuscript, we develop a new mathematical model and associated numerical approximation of the capacitance signaling from DNA origami nanostructures introduced in [11]. While [11] suggests a model for capacitance of the nanostructure pictured in Figure 1, it is unable to easily capture the dynamics of arbitrary nanostructure shapes and fails to consider the full dynamics between the nanostructure and ions suspended in solution. We also find that treating the entire nanostructure as a capacitor as in [11] may not be fully representative of the system. We therefore develop a more thorough model, beginning from the approximation of the electric potential and using differential capacitance to estimate the signal from arbitrary nanostructure shapes, thus paving the way for optimal design investigations of the nanostructures, as their shape and dimension are expected to affect signal strength. Moreover, this work contributes a first step towards uncertainty quantification of device measurements, which is particularly significant for the fields in which it is applied such as medical diagnoses, food safety, and biosurveillance. Section 2 describes our model of a single DNA origami nanostructure and the surrounding electrochemical processes. Nonsmooth and smooth representations of the nanostructure are detailed. Numerical methodology is discussed in Section 3. Section 4 then gives results comparing the nonsmooth and smooth representations of the nanostructure and shows parameter studies to demonstrate the effect of modeling choices on capacitance. Preliminary observations on device sensitivity according to nanostructure design are given in Section 5. Section 6 presents closing remarks and observations.

2. Mathematical model

We employ a continuum model to describe the electrochemical phenomena within the device chamber because the relative size of ions, angstroms, is significantly smaller than that of the DNA origami nanostructure, nanometers. Both the Poisson-Nernst-Planck (PNP) and the Poisson-Boltzmann (PB) equations are well-known mean-field models that approximate an electric potential under an applied field and the associated electric double layer, composed of the Stern and diffuse layers, that forms, seeing various applications within biological phenomena such as in membrane channel and electrokinetic flow models [24–26]. The PNP equations are time dependent and couple the mass conservation of ion concentrations to Gauss's law for the electric potential. Ion concentrations influence the electric potential through a charge density term in Gauss's law, and the electric potential influences ion concentrations through an electromigration term in the flux of the mass conservation equations [27]. On the other hand, the PB equation is steady state and takes ion concentrations to be functions of the electric

potential [28–30]. We use this equation in our model because the nanostructure's reshaping takes place over multiple seconds, in stark contrast to the nanosecond reaction time of ions, thus allowing us to pursue steady state solutions to a discrete sequence of nanostructure positions within its transmutation to approximate signaling. Moreover, the PB equation easily incorporates steric effects by way of force balancing to derive the modified Poisson Boltzmann (mPB) equation, as demonstrated in [31]. Then, with the defined electric potential, differential capacitance is used to determine the capacitance of the electric double layer within the system. For clarity, dimensional parameters throughout this manuscript are marked with a tilde.

2.1. Governing equations

Consider the two-dimensional domain $\tilde{\mathbf{x}} = (\tilde{x}, \tilde{y}) \in \tilde{\Omega} = [\tilde{x}_a, \tilde{x}_b] \times [0, \infty)$ and assume periodicity in $\tilde{x}$. Place a single nanostructure 0.6 nm above an unpassivated bottom surface $\tilde{y} = 0$, centered in $\tilde{x}$, and rotated such that its width aligns with the $\tilde{z}$ axis and its reshaping movement, in which the nanostructure changes angle θ between its arms, is entirely captured in the $\tilde{x} - \tilde{y}$ plane, as demonstrated in Figure 2. The nanostructure is positioned to hover above the bottom surface as it sits upon tiny silts in experiments [11]. These stilts, as well as the nanostructure's hinge and aptamers, are short, single strand DNA tethers. Their effect on the electric field is negligible in comparison to that of the entire DNA origami nanostructure due to their significantly smaller size, and are therefore excluded from the model. The nanostructure's angle will vary between $\theta = 0$ radians and $\theta = \frac{\pi}{2}$ radians; it should be noted that at angle $\theta = 0$, the nanostructure's top and bottom arms are separated by a distance of 1.2 nm. We include this range of angles because tethers can be made so as to keep the nanostructure at such a small angle, and the nanostructure's top arm may open as wide as $\theta = \frac{\pi}{2}$ when untethered.

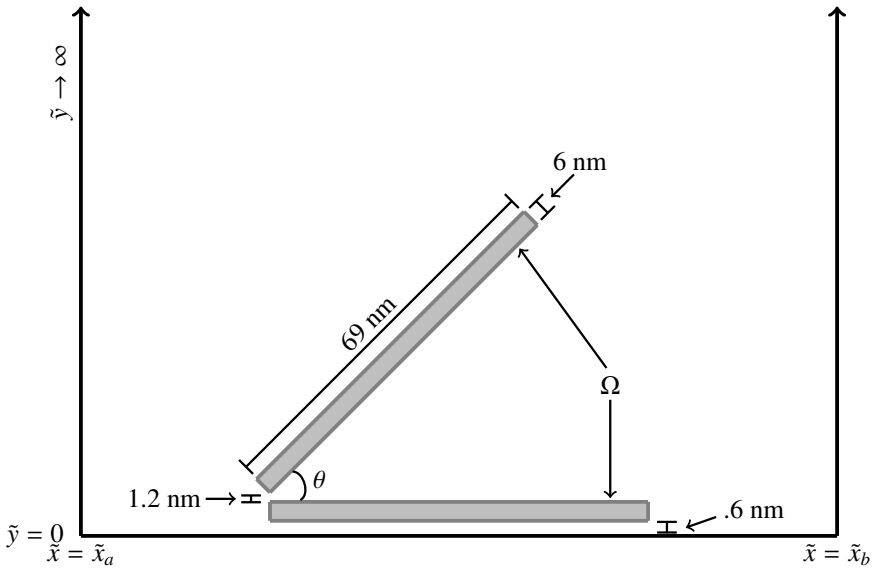


Figure 2. Schematic of modeled domain (not to scale).

The electric potential $\tilde{\phi} = \tilde{\phi}(\tilde{\mathbf{x}})$ obeys Gauss's law:

$$\tilde{\nabla} \cdot (\tilde{d}\tilde{\nabla}\tilde{\phi}) = -\tilde{\rho}, \tag{2.1}$$

where $\tilde{\nabla} = \left[\frac{\partial}{\partial \tilde{x}} \ \frac{\partial}{\partial \tilde{y}}\right]^T$, $\tilde{d} = \tilde{d}(\tilde{\mathbf{x}})$ represents permittivity throughout the domain, and

$$\tilde{\rho} = \sum_{i=1}^{N_{ions}} z_i \tilde{F} \tilde{C}_i + \tilde{P} \tag{2.2}$$

for Faraday's constant $\tilde{F}$, number of ions N_{ions}, integral valence and concentration of i^{th} species of ion z_i and $\tilde{C}_i = \tilde{C}_i(x, y)$, and auxiliary charge function $\tilde{P} = \tilde{P}(\tilde{\mathbf{x}})$. The nanostructure contributes to the system through variability of $\tilde{d}$ and $\tilde{P}$ according to its location in the domain, more thoroughly defined in the following subsection. Therefore, charge density $\tilde{\rho}$ can be seen as the total charge of each ion species accompanied by the background charge of the nanostructure.

The potential $\tilde{\phi}$ is taken to be periodic in $\tilde{x}$, assuming sufficiently wide domain bounds $\tilde{x}_a, \tilde{x}_b$, and a Dirichlet condition, $\tilde{\phi}(\tilde{x}, 0) = \tilde{\phi}_0$, represents the applied voltage on the bottom surface. The potential decays exponentially outside of the electric double layer, so it may be assumed that $\tilde{\phi}$ approaches zero as $\tilde{y}$ tends to infinity. Ion concentrations $\tilde{C}_i$ approach their constant bulk value $\tilde{C}_i^{\infty}$ in this limit as well.

A definition for $\tilde{C}_i$ may be derived by balancing relevant ion forces in equilibrium [31]. Prominent forces are the electrostatic force

$$\tilde{\mathbf{F}}_i^{elec} = -z_i \tilde{e} \tilde{\nabla} \tilde{\phi}, \tag{2.3}$$

for elementary charge $\tilde{e}$, and thermal force

$$\tilde{\mathbf{F}}_i^{therm} = -\tilde{k}\tilde{T}\tilde{\nabla} \ln\left(\tilde{C}_i\right), \tag{2.4}$$

where $\tilde{k}$ is the Boltzmann constant and $\tilde{T}$ is temperature. We also opt to include the Born force,

$$\tilde{\mathbf{F}}_i^{Born} = -\frac{z_i^2 \tilde{e}^2}{8\pi \tilde{R}_i} \tilde{\nabla}\left(\tilde{d}^{-1}\right), \tag{2.5}$$

where R_i is the hydrated radius of ion species i, in which ions are pushed away from areas of low permittivity in order to lower their electrostatic potential energy [32]. This force is particularly important to ensure that the full effect of the DNA origami nanostructure is represented, since its permittivity is an order of magnitude smaller than that of the surrounding water. While permittivity varies within the electric double layer, these variations are negligible compared to that of the nanostructure, and are therefore omitted from our model. Lastly, we add a steric force to limit ion crowding according to the Bikerman model [33],

$$\tilde{\mathbf{F}}_i^{Biker} = -\tilde{k}\tilde{T}\tilde{\nabla} \ln\left(\frac{1 - \sum_{i=1}^{N_{ions}} \frac{\tilde{C}_i^{\infty}}{\tilde{C}_i^{\max}}}{1 - \sum_{i=1}^{N_{ions}} \frac{\tilde{C}_i}{\tilde{C}_i^{\max}}}\right), \tag{2.6}$$

for maximum ion concentrations $\tilde{C}_i^{\max}$, which are calculated from the solubility limits of their associated dissolved salts NaCl and $MgCl_2$, taking the maximum should there be two values as in the case of Cl^-. Other models often use hydrated radii of ions to estimate $\tilde{C}_i^{\max}$, which assumes that hydrated ions are well-modeled as spheres and that $\tilde{C}_i^{\max}$ may be reasonably approximated by the maximum density in which these spheres can exist [31, 34]. The best estimation of $\tilde{C}_i^{\max}$ remains unclear; model effects from variability in this parameter are examined in Section 4.2.

The sum of these forces in equilibrium,

$$\tilde{\mathbf{F}}_i^{Biker} + \tilde{\mathbf{F}}_i^{Born} + \tilde{\mathbf{F}}_i^{elec} + \tilde{\mathbf{F}}_i^{therm} = \mathbf{0}, \tag{2.7}$$

in conjunction with far field condition

$$\lim_{\tilde{y}\to\infty} \tilde{C}_i = \tilde{C}_i^{\infty}, \qquad i = 1, ..., N_{ions}, \tag{2.8}$$

yields a functional relationship expressing $\tilde{C}_i$ in terms of $\tilde{\phi}$, which, when substituted into (2.1), gives our employed mPB equation.

The model is nondimensionalized according to a chosen characteristic length scale $\tilde{L}$, nonzero applied voltage $\tilde{\phi}_0$, and ionic strength $\tilde{I}_c = \frac{1}{2}\sum_i^{N_{ions}} z_i^2 \tilde{C}_i^{\infty}$. To avoid ill conditioning, we only consider applied voltages of $|\tilde{\phi}_0| \geq 0.01$ V and use at least 12.5 mM of $MgCl_2$ in each computation, although other choices of nondimensionalization enable the use of lower values in either parameter. The choice of $MgCl_2$ will remain constant throughout this manuscript, as it was employed as part of a buffer solution in [11]. We will vary the bulk concentration of NaCl between 50 mM and 1 M out of interest motivated by experimental data varying the concentration of suspended electrolytes to observe the impact on sensor signal [35]. Relevant dimensional parameters are listed in Table 1, ion dependent parameters in Table 2, and dimensionless parameters in Table 3; parameters whose tilde has been dropped are understood to be corresponding nondimensional counterparts. The governing nondimensional mPB equation is as follows:

$$\nabla \cdot (\varepsilon \nabla \phi) = -\sum_{i=1}^{N_{ions}} z_i C_i - P, \tag{2.9}$$

where

$$C_i(\mathbf{x}; \phi) = \frac{C_i^{\infty} e^{B_i(1/\varepsilon_w - 1/\varepsilon)} e^{-z_i v \phi}}{1 + \sum_{i=1}^{N_{ions}} \frac{C_i^{\infty}}{C_i^{\max}} \left(e^{B_i(1/\varepsilon_w - 1/\varepsilon)} e^{-z_i v \phi} - 1 \right)}, \tag{2.10}$$

is derived from solving (2.7) and (2.8). Boundary conditions on the electric potential are

$$\phi(x_a, y) = \phi(x_b, y), \tag{2.11a}$$

$$\phi(x, 0) = 1, \tag{2.11b}$$

$$\lim_{y\to\infty} \phi = 0. \tag{2.11c}$$

Differential capacitance,

$$\tilde{c} = \frac{d\tilde{\sigma}}{d\tilde{\phi}_0} \tag{2.12}$$

for bottom surface charge $\tilde{\sigma} = \tilde{\sigma}(\tilde{x}; \tilde{\phi}_0)$ along $\tilde{y} = 0$, is often used to calculate capacitance from electric double layer models [36–38]. This formulation also holds in our model regardless of the DNA origami nanostructuree, an argument for which is given in Appendix A since this result juxtaposes that from [11]. We can therefore interpret the nanostructure's capacitance signaling as its aptitude to disrupt the formation of the electric double layer.

Table 1. Relevant dimensional parameters. Note that $\tilde{\phi}_0$ and $\tilde{I}_c$ will be varied throughout this manuscript so are given as approximate ranges.

Dimensional parameters			
Parameter	Description	Units	Value
$\tilde{\phi}_0$	Applied voltage	V	$O(10^{-1})$
$\tilde{I}_c$	Ionic strength	mol/m^3	$[O(10), O(10^3)]$
$\tilde{L}$	Characteristic length scale	m	40×10^{-9}
$\tilde{F}$	Faraday's constant	C/mol	9.6485×10^4
$\tilde{k}$	Boltzmann constant	m^{2}kg/(s^{2}K)	1.3806×10^{-23}
$\tilde{e}$	Elementary charge	C	1.6022×10^{-19}
$\tilde{R}$	Molar gas constant	J/(K $\cdot$ mol)	8.3144
$\tilde{T}$	Temperature	K	298.15
$\tilde{d}_w$	Permittivity of water	F/m	6.9381×10^{-10}
$\tilde{d}_{DNA}$	Permittivity of DNA	F/m	7.8335×10^{-11}
$\tilde{p}$	Charge density of DNA	C/m^3	-1.474×10^8

Table 2. Relevant ion parameters listed for the modeled ions [39].

Ion dependent parameters					
Parameter	Description	Units	Na^+	Cl^-	Mg^{2+}
z_i	Valence	-	1	-1	2
R_i	Hydrated radius	m	3.6×10^{-10}	3.3×10^{-10}	4.3×10^{-10}
$\tilde{C}_i^{\max}$	Max concentration	M	6.16	17.6	5.7

Table 3. Relevant dimensionless parameters and their formulae.

Dimensionless parameters			
Parameter	Definition	Parameter	Definition
x	$\frac{\tilde{x}}{\tilde{L}}$	C_i	$\frac{\tilde{C}_i}{\tilde{I}_c}$
y	$\frac{\tilde{y}}{\tilde{L}}$	C_i^{∞}	$\frac{\tilde{C}_i^{\infty}}{\tilde{I}_c}$
ϕ	$\frac{\tilde{\phi}}{\tilde{\phi}_0}$	$C_i^{\max}$	$\frac{\tilde{C}_i^{\max}}{\tilde{I}_c}$
v	$\frac{\tilde{\phi}_0 \tilde{F}}{\tilde{R}\tilde{T}}$	$\varepsilon_{w,DNA}$	$\frac{\tilde{\phi}_0 \tilde{d}_{w,DNA}}{\tilde{L}^2 \tilde{F} \tilde{I}_c}$
p	$\frac{\tilde{p}}{\tilde{F}\tilde{I}_c}$	B_i	$\frac{z_i^2 \tilde{e}^2 \tilde{\phi}_0}{8\pi \tilde{R}_i \tilde{k} \tilde{F} \tilde{T} \tilde{L}^2 \tilde{I}_c}$

For our two-dimensional model, capacitance is computed as an integral over x,

$$\tilde{c}_T = \int_{\tilde{x}_a}^{\tilde{x}_b} \frac{d\tilde{\sigma}}{d\tilde{\phi}_0} d\tilde{x}, \tag{2.13}$$

where $\tilde{\sigma}$ is determined by

$$\tilde{\nabla}\tilde{\phi}(\tilde{x}, 0^+) - \tilde{\nabla}\tilde{\phi}(\tilde{x}, 0^-) = -\frac{\tilde{\sigma}(\tilde{x}; \tilde{\phi}_0)}{\tilde{d}}\mathbf{n}, \tag{2.14}$$

and $\mathbf{n} = [0\ 1]^T$, such that the condition reduces to

$$\tilde{\sigma}(\tilde{x}; \tilde{\phi}_0) = -\tilde{d}\ \partial_{\tilde{y}}\tilde{\phi}(\tilde{x}, 0^+), \tag{2.15}$$

as $\tilde{\phi}$ can be taken to be zero outside of the domain. To mimic capacitance from an entire device, we multiply (2.13) by a scaling factor, $\tilde{A} = \frac{0.25\pi\times10^{-7}}{\tilde{x}_b - \tilde{x}_a}$ m, which brings the total bottom surface area to $0.25\,\pi\times10^{-7}$ m^2, the assumed size of the functionalized surface. It should be noted that this calculation assumes the chip is flat and that the nanostructures' size and coverage over the surface is uniform. Moreover, capacitance variation due to device readout effects is not considered.

2.2. Nanostructure treatments

While DNA is fantastically complex, such intricacies are likely be lost in the device's capacitance signaling, as information is only taken from the bottom surface (see Section 2.1 and Appendix A for further details). We therefore take a more general capture of the nanostructure's effect, consequently avoiding numerical challenges posed by the many large negative charges from the phosphate groups positioned along each DNA strand's backbone, as well as the substantial, frequent jumps in permittivity between regions of DNA and water within the nanostructure [40].

We extend an average of the nanostructure's contributed charge and permittivity to two bounding polygons representing its arms, through which ions are permitted to move freely since the ions considered here are smaller in size than the gaps within DNA helices. As DNA's negative charge is derived from phosphate groups along its backbone, we may compute the nanostructure's charge density by multiplying the value of an elementary charge by the anticipated volume of phosphate groups on relaxed double strand DNA per nm^3; this value is given as $\tilde{p}$ in Table 1. The permittivity of the nanostructure is taken to be that of DNA [41].

For the nondimensional model (2.9), we define the following:

$$P = \begin{cases} p, & \mathbf{x} \in \Omega_{DNA}, \\ 0, & \text{else} \end{cases}, \tag{2.16}$$

where Ω_{DNA} is the combined domain of both bounding polygons, and

$$\varepsilon = \begin{cases} \varepsilon_{DNA}, & \mathbf{x} \in \Omega_{DNA}, \\ \varepsilon_w, & \text{else} \end{cases}, \tag{2.17}$$

for $p, \varepsilon_{DNA}, \varepsilon_w$ defined in Table 3.

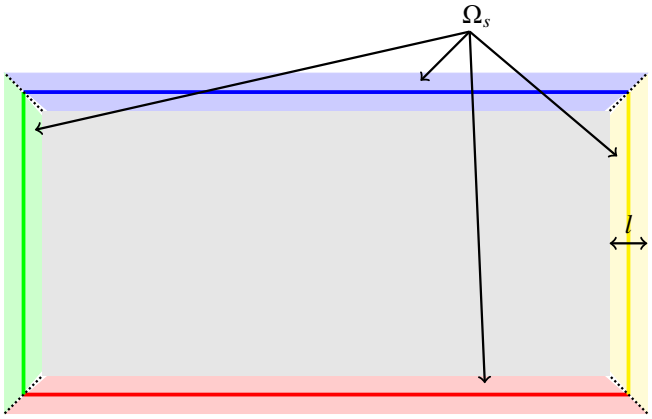


Figure 3. Smoothing regions for an example rectangle. The rectangle boundaries are shown in red, yellow, blue, and green, which outline Ω_{DNA}. The associated smoothing region of each rectangle segment is highlighted in the corresponding lighter color (e.g. the light red region corresponds to the red segment). The smoothing regions are separated along diagonal axes highlighted by the black dotted lines.

Moderate expansion and contraction of the nanostructure has, however, been observed, with each DNA strand expanding up to 0.4 nm [42]. Motivated by this vibrational movement, we define smooth versions of the charge and permittivity functions to account for the effective smearing caused by the motion. Exemplified in Figure 3, we give each segment of the bounding polygons an associated quadrilateral smoothing region extending out by $\frac{l}{2}$ in either normal direction, for maximum vibrational displacement $l = 1.2/\tilde{L}$, and confined by the diagonal axes over which the nanostructure's vibration occurs. Denote these smoothing regions as $\Omega_{s,r}$, $r = 1, 2, ...N_r$ for the total number of segments N_r between the two bounding polygons with $\Omega_s = \Omega_{s,1} \cup \Omega_{s,2} \cup ... \cup \Omega_{s,N_r}$. Also introduce the smoothing function $s = s(\xi_r)$ defined over the interval $\xi_r \in \left[-\frac{l}{2}, \frac{l}{2}\right]$ which satisfies $s\left(-\frac{l}{2}\right) = 1$ and $s\left(\frac{l}{2}\right) = 0$, where mapping $\xi_r = \xi_r(x, y)$ is uniquely defined by each $\Omega_{s,r}$ with $\xi = -\frac{l}{2}$ aligned with the quadrilateral edge inside the bounding polygon. Then, the smooth nanostructure treatment is defined by

$$P_s = \begin{cases} p, & \mathbf{x} \in \Omega_{DNA} \setminus \Omega_s, \\ ps(\xi), & \mathbf{x} \in \Omega_s, \\ 0, & \text{else} \end{cases}, \tag{2.18a}$$

$$d_s = \begin{cases} d_{DNA}, & \mathbf{x} \in \Omega_{DNA} \setminus \Omega_s, \\ (d_{DNA} - d_w)\, s(\xi) + d_w, & \mathbf{x} \in \Omega_s, \\ d_w, & \text{else} \end{cases}. \tag{2.18b}$$

Should the smoothing regions of the nanostructure's two arms overlap, the maximum values of P_s, d_s is taken. However, it should be noted that with sufficient distance between the two arms, this manuscript takes $1.2/\tilde{L}$, any overlap will occur near $\xi_r \approx \frac{l}{2}$ so the effect will be near negligible. It is to be understood that P_s, d_s replace P, d in the governing equation (2.9) to enact the smoothing treatment of the nanostructure. Without loss of generality, we use the nonsmooth treatment in the description of numerical methodology in the subsequent section.

Since non-smooth forcing functions and variable coefficients can cause accuracy to be lost in numerical implementation, the smooth nanostructure treatment will have computational advantages over the non-smooth treatment. In such instances, jump capturing schemes may be used to maintain the order-of-accuracy of the method even with discontinuities over interfaces [43]. It is unclear, however, that the difference in nanostructure treatment will have a significant impact on the approximation of capacitance, since it is calculated only from information along the bottom surface, potentially sheltered from introduced numerical error along the nanostructure. Differences between the nanostructure treatments are investigated in Section 4.1.

3. Numerical methodology

We opt to truncate the computational domain in y since the electric potential will rapidly decay from the bottom surface, therefore introducing y_b, taken to be sufficiently far from the nanostructure such that the computational domain is $[x_a, x_b] \times [0, y_b]$ and the upper boundary condition is $\phi(x, y_b) = 0$. Discretize the computational domain with a uniform Cartesian grid, taking $h_x = h_y = h > 0$ to be the grid cell size such that $\mathbf{x_j} = (x_a + j_x h,\ j_y h)$ for multi-index $\mathbf{j} = (j_x, j_y) \in \mathbb{Z}^2$ with $N_x,\ N_y$ number of grid points in each respective direction. The first-order accurate divided differences approximating the first derivative in x are

$$D_{+x} W_{\mathbf{j}} = \frac{W_{\mathbf{j}+\mathbf{e}_x} - W_{\mathbf{j}}}{h}, \tag{3.1a}$$

$$D_{-x} W_{\mathbf{j}} = \frac{W_{\mathbf{j}} - W_{\mathbf{j}-\mathbf{e}_x}}{h}, \tag{3.1b}$$

for arbitrary grid function $W_{\mathbf{j}} \approx W(\mathbf{x_j})$ and $\mathbf{e}_x = (1, 0)$, with the difference operators similarly defined in y, taking $\mathbf{e}_y = (0, 1)$.

Define $\Phi_{\mathbf{j}} \approx \phi(\mathbf{x_j})$, $C_{i,\mathbf{j}} = C_i(\mathbf{x_j}; \Phi_{\mathbf{j}})$, and $P_{\mathbf{j}} = P(\mathbf{x_j})$. The variable coefficient ε will be evaluated at cell edge centers, e.g., $\varepsilon_{\mathbf{j}+\frac{1}{2}\mathbf{e}_x} = \varepsilon(x_{j_x} + \frac{1}{2}h, y_{j_y})$. Then the governing equation (2.9) is discretized on interior grid points as

$$D_{+x}\left(\varepsilon_{\mathbf{j}-\frac{1}{2}\mathbf{e}_x} D_{-x}\Phi_{\mathbf{j}}\right) + D_{+y}\left(\varepsilon_{\mathbf{j}-\frac{1}{2}\mathbf{e}_y} D_{-y}\Phi_{\mathbf{j}}\right) = -\sum_{i=1}^{N_{ions}} z_i C_{i,\mathbf{j}} - P_{\mathbf{j}}, \tag{3.2}$$

where the ion concentrations are evaluated as

$$C_{i,\mathbf{j}} = \frac{C_i^{\infty} e^{B_i(1/\varepsilon_w - 1/\bar{\varepsilon}_{\mathbf{j}})} e^{-z_i \nu \Phi_{\mathbf{j}}}}{1 + \sum_{i=1}^{N_{ions}} \frac{C_i^{\infty}}{C_i^{\max}} \left(e^{B_i(1/\varepsilon_w - 1/\bar{\varepsilon}_{\mathbf{j}})} e^{-z_i \nu \Phi_{\mathbf{j}}} - 1\right)}, \tag{3.3}$$

for $\bar{\varepsilon}_{\mathbf{j}}$ either defined as a function evaluation at grid point $\mathbf{j}$ or an average of the surrounding values at staggered grid points,

$$\bar{\varepsilon}_{\mathbf{j}} = \varepsilon(\mathbf{x_j}), \quad \text{or} \tag{3.4a}$$

$$\bar{\varepsilon}_{\mathbf{j}} = \frac{\varepsilon_{\mathbf{j}-\frac{1}{2}\mathbf{e}_x} + \varepsilon_{\mathbf{j}-\frac{1}{2}\mathbf{e}_y} + \varepsilon_{\mathbf{j}+\frac{1}{2}\mathbf{e}_x} + \varepsilon_{\mathbf{j}+\frac{1}{2}\mathbf{e}_y}}{4}. \tag{3.4b}$$

While the first option is more precise, the latter is second-order accurate and thus maintains the designed order-of-accuracy of (3.2); the decision is therefore based on ease of implementation for the user, this manuscript taking $\bar{\varepsilon}_{\mathbf{j}}$ to be the average. The scheme is completed by boundary conditions

$$\phi_{j_x 0} = 1, \tag{3.5a}$$

$$\phi_{j_x N_y} = 0, \tag{3.5b}$$

$$\phi_{-1 j_y} = \phi_{N_x - 1 j_y}, \tag{3.5c}$$

$$\phi_{N_x j_y} = \phi_{0 j_y}. \tag{3.5d}$$

for ghost point x_{-1}.

Note that in the nonsmooth nanostructure treatment, $\varepsilon_{\mathbf{j}-\frac{1}{2}\mathbf{e}_x}$ and $P_{\mathbf{j}}$ are discontinuous along grid lines rather than the perimeter of Ω_{DNA}, causing a stair-casing effect, which can be minimized with a very fine resolution or entirely avoided by employing the smooth nanostructure treatment. In the smooth treatment, however, the smoothing function s must be chosen such that P_s, ε_s have adequate regularity in the computational domain in order to maintain the designed order-of-accuracy. Specifically, s must be defined such that $P_s, \varepsilon_s \in C^1$, with allowance for small discontinuities in second-order derivatives, and that h is taken sufficiently small such that s is well resolved. We take the cubic function,

$$s(\xi_r) = \frac{1}{2} - \frac{3}{2l}\xi_r + \frac{2}{l^3}\xi_r^3, \tag{3.6}$$

and $h \lesssim l/4$.

An inexact Newton method, detailed in Algorithm 1, is used to solve (3.2), suggested from [44]. Appendix B gives a theoretical analysis showing the expected convergence of the method to a unique solution by demonstrating the existence and uniqueness of a minimizing solution ϕ^* to a related energy functional. For the iteration, we introduce the vector of grid function values $\mathbf{\Phi}^{(k)}$, residual $\mathbf{g}^{(k)}$, Jacobian $J^{(k)}$, search direction $\delta\mathbf{\Phi}^{(k)}$, and step length $\lambda^{(k)}$ for iteration number k.

Algorithm 1 Inexact Newton iteration

Initialize $\mathbf{\Phi}^{(0)}$, $k = 0$, α, and tol.
while $\|\mathbf{g}^{(k)}\|_2 > tol$ **do**
    $\mathbf{g}^{(k)} =$ calculateResidual($\mathbf{\Phi}^{(k)}$).
    $J^{(k)} =$ calculateJacobian($\mathbf{\Phi}^{(k)}$).
    while $\|J^{(k)}\delta\mathbf{\Phi}^{(k)} + \mathbf{g}^{(k)}\|_2 > \alpha\|\mathbf{g}^{(k)}\|_2$ **do** ▷ Begin inner iteration
        Approximate $J^{(k)}\delta\mathbf{\Phi}^{(k)} = -\mathbf{g}^{(k)}$. ▷ E.g. conjugate gradient
    end while ▷ End inner iteration
    $\lambda^{(k)} =$ lineSearch($\mathbf{\Phi}^{(k)}$, $\delta\mathbf{\Phi}^{(k)}$, $\mathbf{g}^{(k)}$). ▷ E.g. backtracking
    Update $\mathbf{\Phi}^{(k+1)} = \mathbf{\Phi}^{(k)} + \lambda^{(k)}\delta\mathbf{\Phi}^{(k)}$.
    $k = k + 1$.
end while

In execution of the algorithm, we take an outer stopping tolerance of $tol = 10^{-8}$ on the L_2 norm of the gradient defined as,

$$\|\mathbf{g}^{(k)}\|_2 = \sqrt{\sum_{j_y=0}^{N_y}\sum_{j_x=0}^{N_x}\left(g_{\mathbf{j}}^{(k)}\right)^2} < tol, \tag{3.7}$$

unless otherwise stated. The inner iteration takes a tolerance relative to the size of $\|\mathbf{g}^{(k)}\|_2$ with $\alpha = 10^{-4}$, and is solved with a conjugate gradient method. The line search uses a backtracking algorithm to satisfy the Armijo condition, in which values for step size $\lambda^{(\kappa)}$ are tested and reduced uniformly until a sufficient decrease in the objective function is observed [45]. The initial guess $\mathbf{\Phi}^{(0)}$ is taken to be the corresponding one-dimensional solution without the DNA origami nanostructure, set constant across x. For efficiency in iteration convergence, the periodic boundary conditions (3.5c), (3.5d) are replaced with Dirichlet conditions applying the corresponding one-dimensional solution, as the two-dimensional solution returns to the one-dimensional solution when sufficiently far from the nanostructure, thus mimicking periodicity.

To approximate capacitance, let $\tilde{c}_{h,j_x} \approx \tilde{c}$ at $\tilde{x}_{j_x}$ on the bottom surface and introduce $\delta\tilde{\phi}_0 > 0$ to be a small step size in $\tilde{\phi}_0$, so (2.12) is discretized as

$$\tilde{c}_{h,j_x} \approx \frac{\tilde{\sigma}_{h,j_x}(\tilde{\phi}_0 + \delta\tilde{\phi}_0) - \tilde{\sigma}_{h,j_x}(\tilde{\phi}_0)}{\delta\tilde{\phi}_0}, \tag{3.8}$$

where $\tilde{\sigma}_{h,j_x}(\tilde{\phi}_0) \approx \tilde{\sigma}(\tilde{x}_{j_x}; \tilde{\phi}_0)$ given $\tilde{\phi}_0$ as

$$\tilde{\sigma}_{h,j_x} = -\tilde{d} D_{+y} \tilde{\Phi}_{j_x 0}. \tag{3.9}$$

Equation (2.13) is then approximated with a Riemann sum; this manuscript employs the midpoint quadrature,

$$\tilde{c}_{T,h} \approx \tilde{A} \sum_{j_x=0}^{N_x-1} \tilde{L} h \left(\frac{\tilde{c}_{h,j_x} + \tilde{c}_{h,j_x+1}}{2} \right). \tag{3.10}$$

4. Model evaluation

Our model must consider a wide range of solutions since biosensing devices scan over a large span of applied voltages, known as a capacitance-voltage (CV) sweep, and future investigations into optimal bulk ion concentrations creates large variability in ionic strength. An example of this range in solution is shown in Figure 4 for cases $\tilde{\phi}_0 = 0.4$ V with 50 mM NaCl and $\tilde{\phi}_0 = 0.01$ V with 1 M NaCl. The first computation shows the solution to be a consistent magnitude throughout the domain, whereas the second exhibits a entire decade difference inside and outside of the nanostructure.

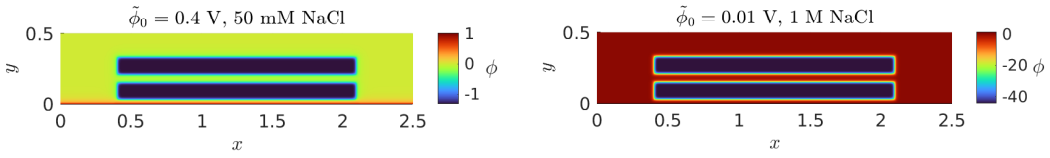


Figure 4. Example numerical solutions highlighting solution variability. Computations took $N_x = 2560$, 12.5 mM $MgCl_2$, $\theta = 0$, and the smoothing treatment of the nanostructure.

Capacitance curves produced by CV sweeps for three different concentrations of NaCl are shown in Figure 5 to serve as a basis of comparison for results given in this section, as we will use CV sweeps to evaluate modeling choices as they engage with the variability in the solution. Cases with and without

the nanostructure are plotted. Capacitance exhibits a double-hump behavior as it sweeps across applied voltage, a phenomenon observed in experiment [35, 46].

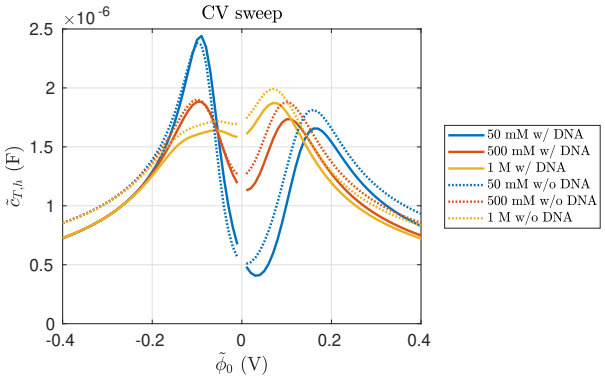


Figure 5. Capacitance curves from CV sweeps calculated with (w/) and without (w/o) the DNA origami nanostructure. Three cases of ionic strength are plotted, given as molarity of NaCl in the legend. Computations took $N_x = 2560$, 12.5 mM $MgCl_2$, $\theta = 0$, and the smoothing treatment of the nanostructure.

Concentrations of salts NaCl and $MgCl_2$ are given to inform the values of $\tilde{C}_i^{\infty}$ and $\tilde{I}_c$ in each study. Unless otherwise stated, it may be assumed that $x_a = 0$, $x_b = 2.5$, $y_b = .5$, $N_x = 2560$, $tol = 10^{-8}$, $\delta\tilde{\phi}_0 = 10^{-5}$, and 12.5 mM of $MgCl_2$ is used. Each study will also include the nanostructure at an angle of $\theta = 0$.

4.1. Comparison of nanostructure treatments

We begin analyzing the use of the nonsmooth and smooth nanostructure treatments by quantifying their respective approximations to the electric potential. Richardson extrapolation is used to estimate the numerical error in the electric potential e_ϕ from successive computations taking $N_x = 1280, 2560$, as well as $N_x = 640, 1280, 2560$ to estimate order-of-accuracy. Estimated errors are represented by the max-norm, or infinity-norm, defined as

$$\|\mathbf{w}\|_\infty = \max_{\mathbf{j}} |w_{\mathbf{j}}|, \tag{4.1}$$

for arbitrary grid function $\mathbf{w}$.

Figure 6 plots e_ϕ across three voltage sweeps of differing ionic strength. The nonsmooth nanostructure treatment admits larger errors than the smooth treatment, and both treatments exhibit the largest errors for voltages of small magnitude, likely due to large solution values produced by nondimensionalization with small $\tilde{\phi}_0$, as seen in Figure 4. The nonsmooth treatment also experiences a loss in accuracy, with some cases of applied voltage near $\tilde{\phi}_0 = -0.4$ V showing a near complete loss, whereas the smooth treatment maintains the designed second-order accuracy. These results, however, are likely attributed to the nanostructure's resolution. Figure 7 plots examples of e_ϕ to demonstrate that in either treatment, maximum errors are associated with the nanostructure.

On the other hand, differential capacitance in our system is calculated only from information along the bottom surface. Figure 8 plots the capacitance curves associated with CV sweeps for each nanostructure treatment and varying ionic strength to observe potential differences. Although each nanos-

tructure treatment shows distinct curves, the general double-hump trend in capacitance is largely preserved, positing that the nonsmooth treatment's large numerical error and loss in order-of-accuracy does not entirely disrupt the precision of the capacitance calculation.

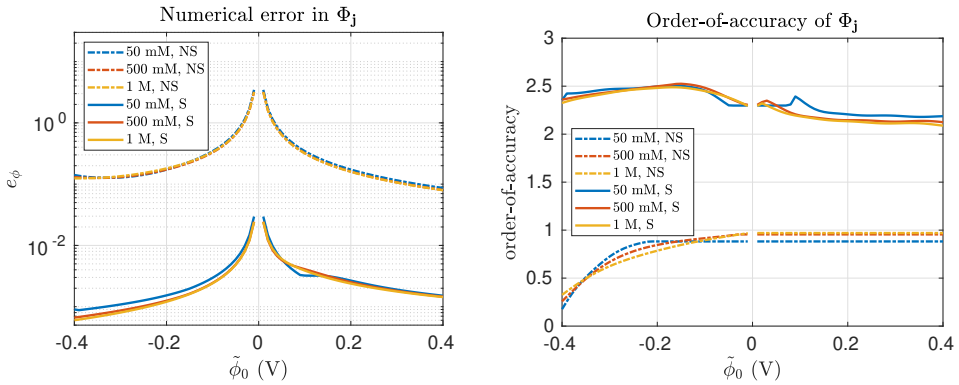


Figure 6. Distribution of e_ϕ (left) and its discretization order-of-accuracy (right) computed across applied voltage and ionic strength, listed as molarity of NaCl in the legend. Results for the smooth nanostructure treatment (S) are plotted in solid lines and the nonsmooth (NS) dashed lines.

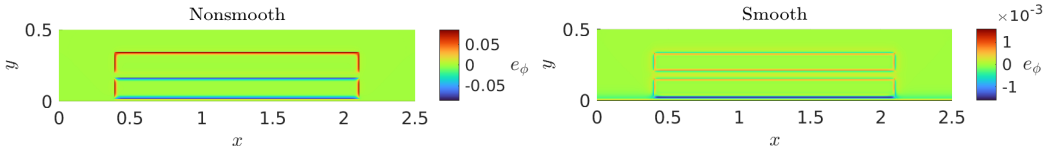


Figure 7. Estimated error e_ϕ associated with $\tilde{\phi}_0 = .4$ V and 50 mM of NaCl for the nonsmooth (left) and smooth (right) nanostructure treatments.

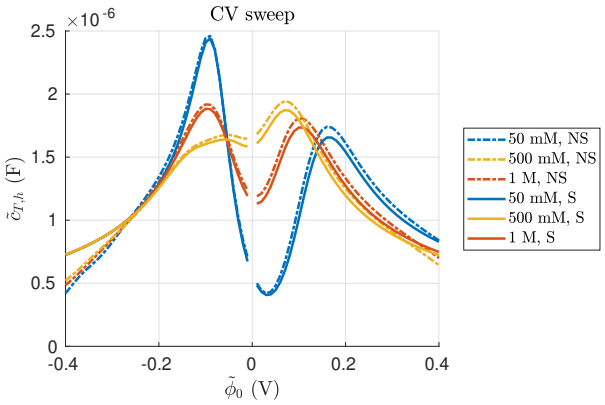


Figure 8. Capacitance calculated with the nonsmooth (NS) and smooth (S) nanostructure treatments as a function of applied voltage and ionic strength, given as molarity of NaCl in the legend.

We also observe that the difference in capacitance between the nanostructure treatments is not entirely derived from discretization accuracy, as Figure 9 plots the relative difference in capacitance

between the two treatments for increasing grid resolution, $|\tilde{c}_{T,h}^{(NS)} - \tilde{c}_{T,h}^{(S)}|/|\tilde{c}_{T,h}^{(S)}|$. The difference between the capacitance calculations changes very little in magnitude throughout the refinement, suggesting that the two nanostructure treatments produce unique capacitance curves that do not converge to one another.

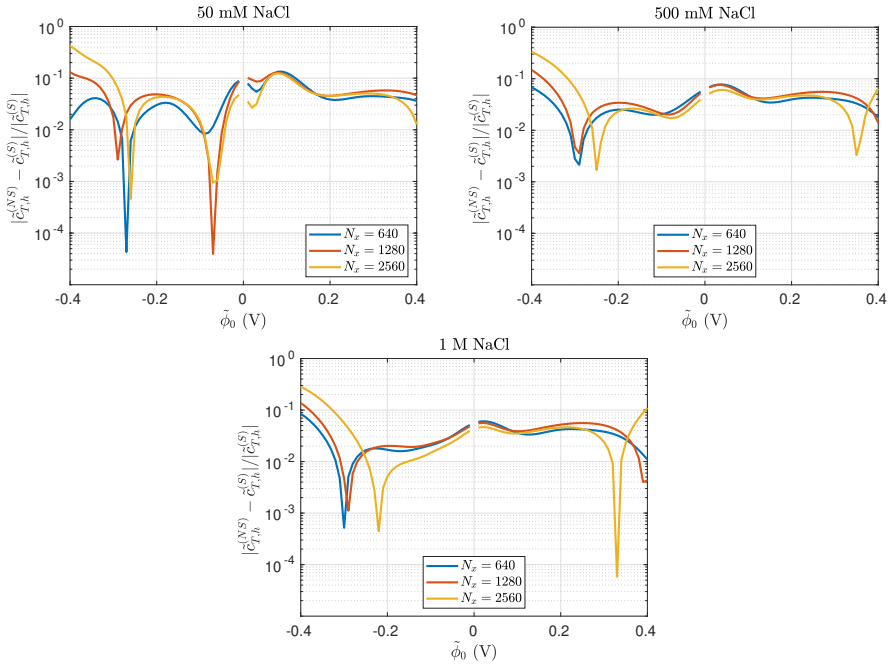


Figure 9. Magnitude of the relative difference between capacitance curves from CV sweeps with the nonsmooth $\left(\tilde{c}_{T,h}^{(NS)}\right)$ and smooth $\left(\tilde{c}_{T,h}^{(S)}\right)$ nanostructure treatments as the computational grid is refined. Three cases of ionic strength are plotted, given as molarity of NaCl in each title.

Instead, we expect that the difference in capacitance is largely an artifact of the nanostructure's vibrational movement and effective smearing in the representations of permittivity and background charge across the computational domain. To illustrate, Figure 10 plots e_ϕ and capacitance curves from CV sweeps as the smoothing length $\tilde{l}$ is decreased, including results from the nonsmooth nanostructure treatment for comparison. We can see that the capacitance curves associated with lower values of $\tilde{l}$ rapidly converge to the capacitance curve associated with the nonsmooth nanostructure treatment. This is especially observed along the hump in the positive voltage range, where capacitance curves with $\tilde{l} = 0.3, 0.6$ nm nearly overlap with that of the nonsmooth nanostructure treatment. While we also see that the numerical error associated with lower values of $\tilde{l}$ also converge to the magnitude of error associated with the nonsmooth nanostructure treatment, it is apparent that this convergence in error is much slower than the convergence in capacitance, except for small intervals of large applied voltage near $|\tilde{\phi}_0| = 0.4$ V, where the rate of convergence appears comparable. This suggests that away from large applied voltages, differences in capacitance between the nonsmooth and smooth nanostructure treatments is not necessarily derived from the nonsmooth treatment's large numerical error, but rather the distance of the nanostructure's vibrational movement. Near large applied voltages, however, the magnitude of numerical error appears to play a stronger role.

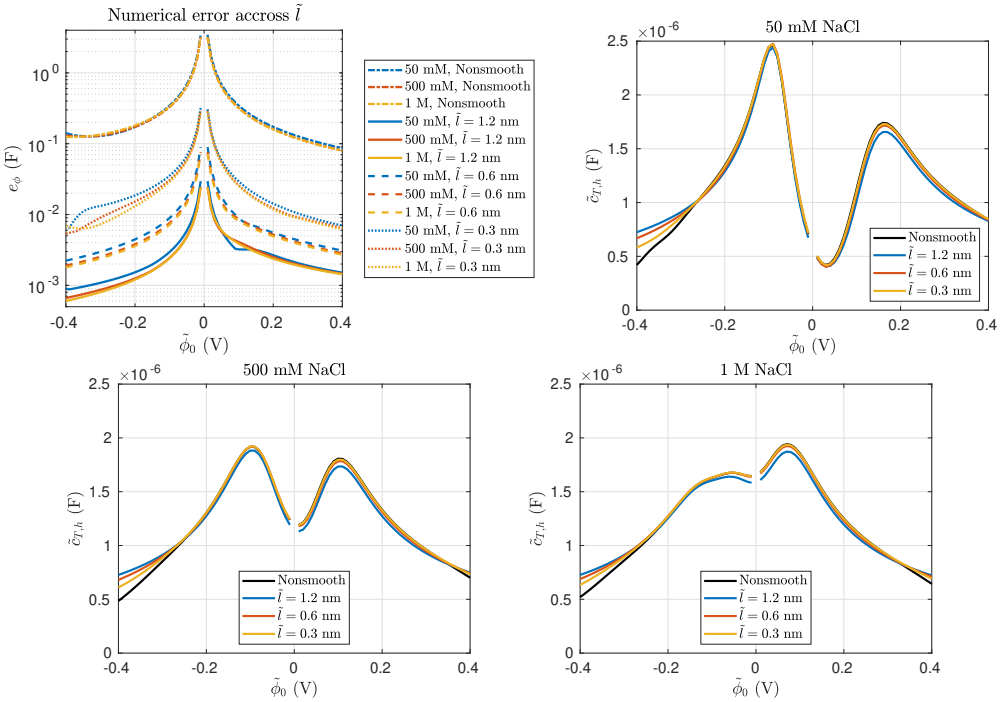


Figure 10. The top left plot shows the estimated numerical error e_ϕ across applied voltage and ionic strength. Computations taking $N_x = 1280, 2560$ were used in the estimation. All other plots show capacitance curves from CV sweeps with decreasing $\tilde{l}$. Three cases of ionic strength are plotted, given as molarity of NaCl in each title. Capacitance curves associated with the nonsmooth nanostructure are plotted in black for comparison.

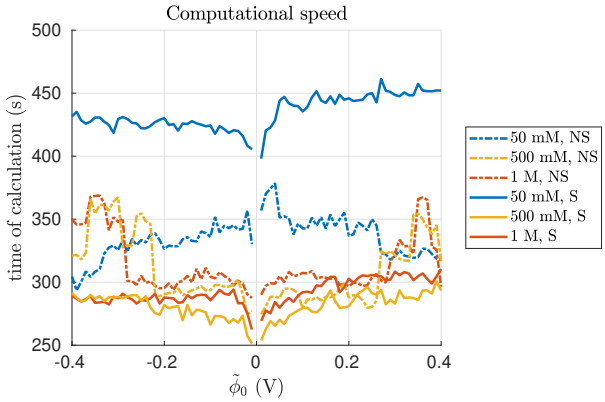


Figure 11. Plot of average time elapsed over five computations for each capacitance calculation across applied voltage and ionic strength, given as molarity of NaCl in the legend. The nonsmooth (NS) nanostructure treatment is plotted with the dashed lines and the smooth (S) treatment is plotted with the solid lines. Computations took $N_x = 2560$, $tol = 10^{-8}$, and $y_b = 0.5$, and were run in serial using an Intel Xeon 3.6GHz processor with the gcc compiler and -O3 optimization flag.

It should be emphasized that this difference in capacitance between the nanostructure treatments is far smaller in magnitude than the difference in e_ϕ, and that without experimental data to inform

modeling performance, one nanostructure treatment cannot be recommended over the other. A brief investigation into computational speed, the results of which are shown in Figure 11, echos our conclusion, finding subtle differences between the nanostructure treatments but no treatment consistently computationally quicker than the other. We therefore leave the choice of nanostructure treatment to the employer, the remainder of this manuscript taking the smooth treatment in all computations.

4.2. Parameter study

We now explore other potential factors than may influence capacitance, beginning with the choice of grid spacing h and perturbation in applied voltage $\delta\tilde{\phi}_0$. Figure 12 plots the estimated relative error in capacitance e_c as h and $\delta\tilde{\phi}_0$ are refined, using Richardson extrapolation to estimate error from successively refined computations across applied voltage and ionic strength. The refinement in h uses $N_x = 640, 1280$ for a coarse mesh error estimation and $N_x = 1280, 2560$ for a fine mesh error estimation. The refinement in $\delta\tilde{\phi}_0$ takes $\delta\tilde{\phi}_0 = 10^{-4}, 10^{-5}$ for a coarse estimation and $\delta\tilde{\phi}_0 = 10^{-5}, 10^{-6}$ for fine. In each case, e_c generally decreases as each parameter is refined; the refinement of $\delta\tilde{\phi}_0$ shows a less consistent decrease due to round off errors since absolute errors begin to tend toward machine precision. We also see that the error associated with h is significantly larger than that of $\delta\tilde{\phi}_0$, suggesting that the numerical error in capacitance may largely be due to error in the approximation of the electric potential and surface charge, unless significant refinement or a higher-order accurate method is used. We suggest a minimum grid resolution $N_x \geq 1500$ to balance the order of associated error $e_c \lessapprox 10^{-1}$ with computational speed. Similarly, we suggest a perturbation in the applied voltage no greater than $\delta\tilde{\phi}_0 \leq 10^{-3}$ for associated errors of magnitude $e_c \lessapprox 10^{-2}$.

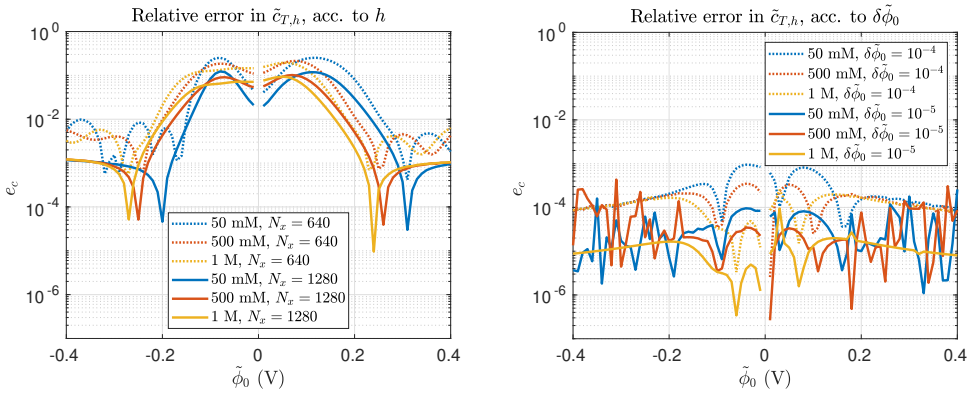


Figure 12. Distribution of e_c according to h (left) and $\delta\tilde{\phi}_0$ (right) computed across applied voltage and ionic strength, listed as molarity of NaCl in the legend. Absolute errors may be thought of the relative error multiplied by a factor of 10^{-6}.

To further evaluate potential influences on capacitance, we turn our attention to the presence of auxiliary ions in our model. Experiments often include other salts, molecules, and ions to maintain a controlled environment, an example of which is phosphate-buffered saline (PBS) that is used to control the pH level. Figure 13 shows capacitance curves from CV sweeps including zero, half, and full concentration of Dulbecco's PBS, recipes for which are given in Table 4 and relevant ion parameters in Table 5. Despite its use as a buffer solution, the inclusion of the auxiliary ions in our model greatly influences capacitance, especially in the positive voltage range where negatively charged ions HPO_4^{-2}

and $H_2PO_4^-$ entirely reshape the curves, regardless of their small bulk concentrations. Our model therefore strongly suggests accounting for any charged ion present in solution.

Table 4. List of salts and their respective concentrations for full and half concentration of Dulbecco's PBS.

PBS recipe		
Salt	Full concentration (mM)	Half concentration (mM)
Na_2HPO_4	8.1	4.05
KH_2PO_4	1.5	0.75
NaCl	137	68.5
KCl	2.7	1.35

Table 5. Relevant ion parameters listed for the modeled ions [39].

Ion dependent parameters for PBS					
Parameter	Description	Units	HPO_4^{-2}	$H_2PO_4^-$	K^+
z_i	Valence	-	-2	-1	1
R_i	Hydrated radius	m	3.27×10^{-9}	3.02×10^{-10}	2.01×10^{-10}
$\tilde{C}_i^{\max}$	Max concentration	M	.2872	1.6618	4.5576

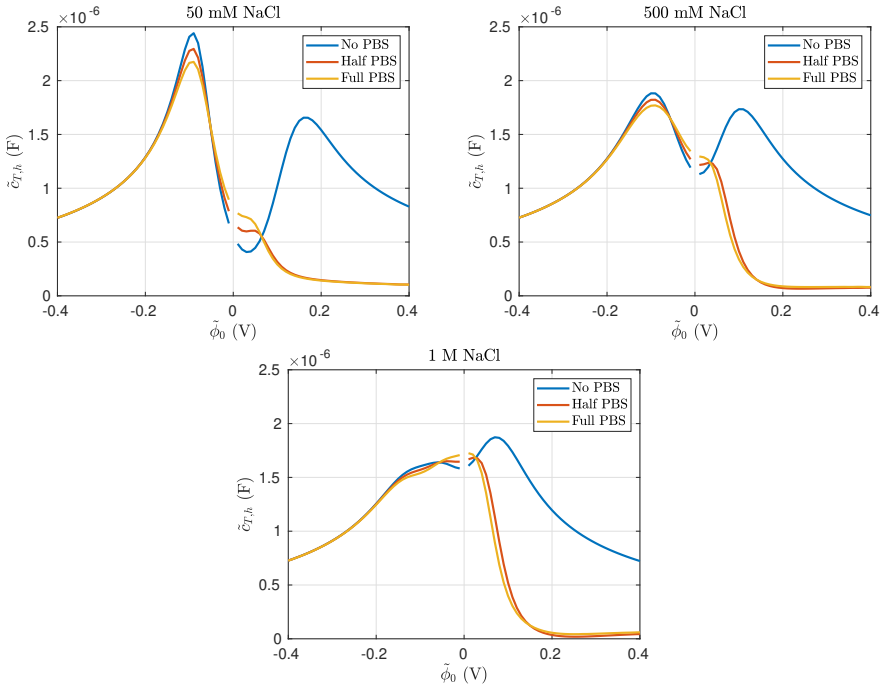


Figure 13. Capacitance curves from CV sweeps calculated with no, half-concentration, and full-concentration of PBS. Three cases of ionic strength are plotted, given as molarity of NaCl in each plot title.

Lastly, we investigate the effect of variability within maximum ion concentrations by changing these values according to a multiplicative factor $\gamma > 0$, taking $\gamma \tilde{C}_i^{\max}$ in computations. Figure 14 plots these

results, finding a moderate effect on the magnitude and shape of capacitance. While the double hump behavior is preserved, the location and magnitude of the humps evolves as a function of γ. Note that defining $\tilde{C}_i^{\max}$ according to hydrated radii as done in [31, 34] corresponds to $\gamma > 2.5$, with variations for each ion. Thus, proper estimation of $\tilde{C}_i^{\max}$ is an important feature of our model, optimally set by measurement or alternatively fit by way of comparison to experimental data.

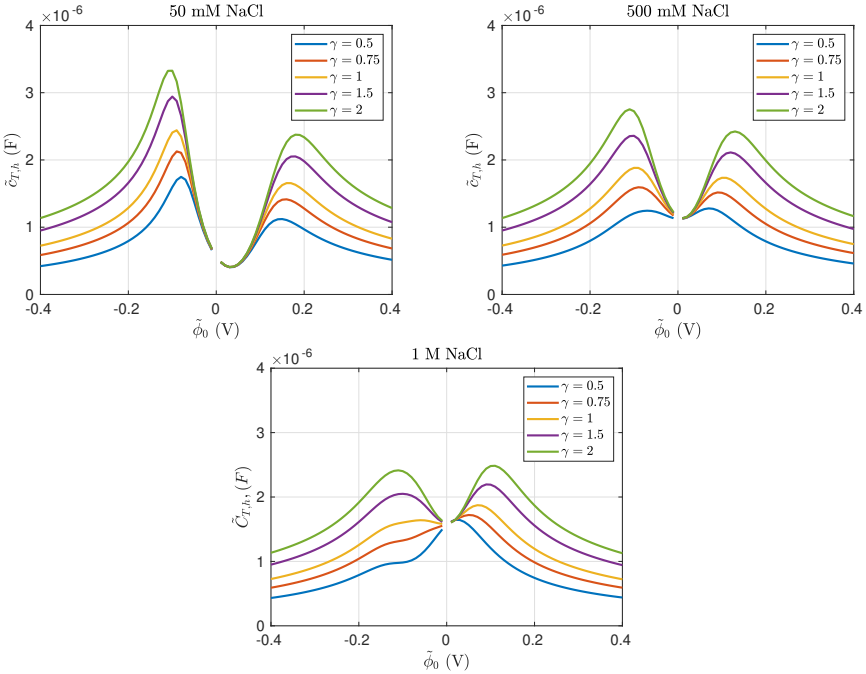


Figure 14. Capacitance curves from CV sweeps calculated with different values of γ. Three cases of ionic strength are plotted, given as molarity of NaCl in each plot title.

5. Device design

Using our model, we now make observations and suggestions on nanostructure design according to the potential impact on device sensitivity. We consider the height of the nanostructure stilts as well as the signal of three candidate nanostructure shapes across applied voltage and ionic strength.

5.1. Nanostructure stilt height

In experiments, DNA origami nanostructures resides on stilts that attach to the bottom surface, the height of which may be chosen. Since the capacitance signal of the biosensing device corresponds to the nanostructure's ability to disrupt the electric double layer, which itself is only a few nanometers in length from the bottom surface, we expect that the stilts can only be made so high before losing device sensitivity. Figure 15 plots the difference in capacitance between a computation with a stilt height of $\tilde{S}_H$ and a computation without the nanostructure, previously shown in Figure 5, which we will call $\Delta\tilde{c}_{T,h}^{(\tilde{S}_H)}$. We see that $\Delta\tilde{c}_{T,h}^{(\tilde{S}_H)}$ decreases as stilt height increases, and especially so for cases of higher ionic strength. This suggests that capacitance curves with increasing stilt height converge to that without the nanostructure, indicating that device sensitivity may be lost if the stilts are taken too high.

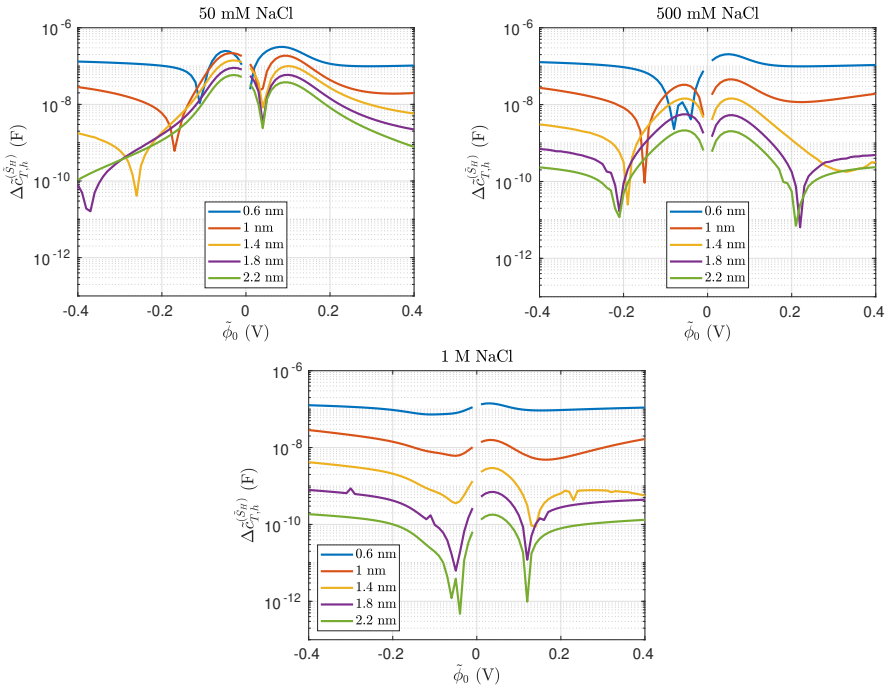


Figure 15. Difference in capacitance between a computation of stilt height $\tilde{S}_H$ and a computation without the DNA origami nanostructure. Values in the legend are provided in nanometers.

To build confidence within these results, Figure 16 plots the estimated error in $\Delta\tilde{c}_{T,h}^{(\tilde{S}_H)}$ as the computational grid is refined, using Richardson extrapolation to compute error for a coarse grid ($N_x = 2000, 2500$) and fine grid ($N_x = 2500, 3000$) for the cases of $\tilde{S}_H = 1$ nm and 500 mM of NaCl pictured in the left plot and $\tilde{S}_H = 1.8$ nm and 1 M of NaCl in the right plot. The estimated errors are significantly lower, on the order of 10^{-11}, than the magnitude of the result shown in Figure 15, on the order of 10^{-9}, demonstrating the robustness of the result.

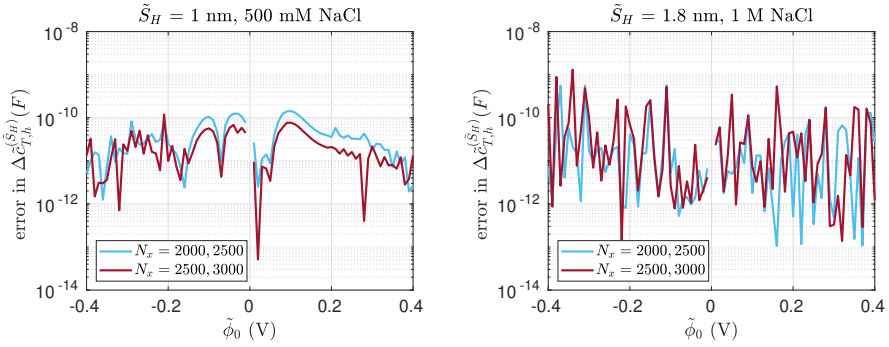


Figure 16. Estimated error in $\Delta\tilde{c}_{T,h}^{(\tilde{S}_H)}$ for the case of $\tilde{S}_H = 1$ nm and 500 mM of NaCl (left) as well as $\tilde{S}_H = 1.8$ nm and 1 M of NaCl (right). Error for a coarse grid, computed with $N_x = 2000, 2500$ and a fine grid, $N_x = 2500, 3000$, are shown.

5.2. *Nanostructure shape*

Three candidate nanostructure shapes are shown in Figure 17, which we will refer to as the *original*, *hammer*, and *single arm* designs. The original and hammer designs are constructed such that the nanostructure's upper arm opens from $\theta = 0$ to $\theta = \frac{\pi}{2}$ radians to indicate signaling. The single arm structure moves in the same manner, relative to the bottom surface. Nanostructure dimensions are taken from Figure 2; the length of the bottom arm in the hammer design in taken to be 30 nm.

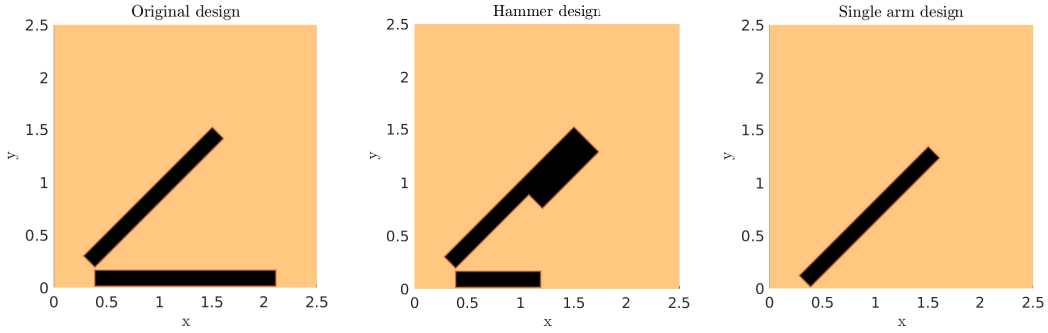


Figure 17. The three candidate nanostructure designs, shown at $\theta = \frac{\pi}{4}$.

We approximate nanostructure signaling by computing steady state solutions to a discrete set of nanostructure angles, discretized as $\theta_\tau = \tau\delta\theta$ for index $\tau = 0, 1, ..., N_\tau$, number of angles N_τ, and angle step size $\delta\theta$. The left plot in Figure 18 shows the capacitance signal of the three nanostructure shapes for $N_\tau = 45$, $N_x = 1500$, $y_b = 2.5$, 50 mM of NaCl, 12.5 mM of $MgCl_2$, and an applied voltage of $\tilde{\phi}_0 = 0.05$ V. The single arm design shows the largest change in capacitance as it signals, whereas the original design shows nearly no change. This difference is likely caused by the stagnant position of the bottom arm in the original design, since the electric double layer would remain rather consistent regardless of the position of the top arm. In the single arm and hammer designs, a large portion of the nanostructure is effectively removed from interfering with the electric double layer as it signals, which, as a result drastically changes the double layer's formation, as observed by the change in capacitance. The right plot in Figure 18 shows the capacitance signal of the single arm design as the computational grid is refined, taking $N_x = 1500, 2000, 2500, 3000$. We see that the general behavior of the nanostructure's signal remains as its magnitude converges towards its true value.

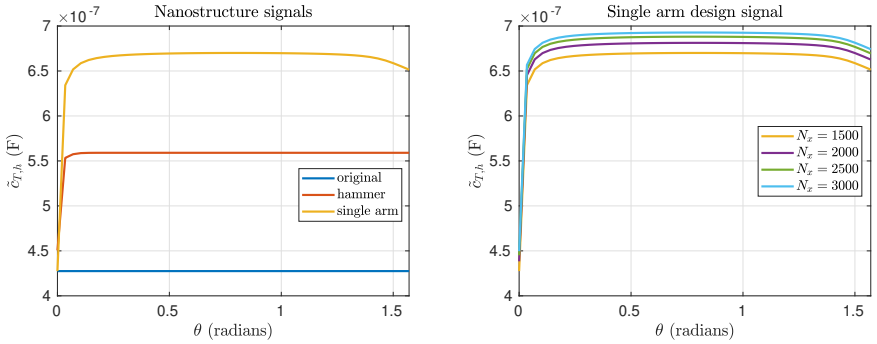


Figure 18. LEFT: Example capacitance signal of each nanostructure design over the range of nanostructure angle. RIGHT: Capacitance signal of the single arm design as the computational grid is refined.

Additionally, we observe that the bulk of each design's signal is captured within a small range of angle. This is computationally advantageous, as we may only consider two nanostructure positions that are close in angle to approximate the resulting signal; it should be noted that the nanostructure's stilt height likely influences the range of angle. The left plot in Figure 19 shows the representation of each design's signal as the difference in capacitance between $\theta_0 = 0$ and $\theta_1 = \frac{\pi}{40}$ across a CV sweep for varying ionic strength. In this result, $N_x = 2560$ is taken. First, we observe that the original design exhibits nearly no change in capacitance as it signals, and that the single arm design produces a signal about twice as large as the hammer design. The right plot in Figure 19 shows the signal of the single arm nanostructure as the computational grid is refined, taking $N_x = 1500, 2000, 2500$, demonstrating the robustness of the observed signal to computational changes.

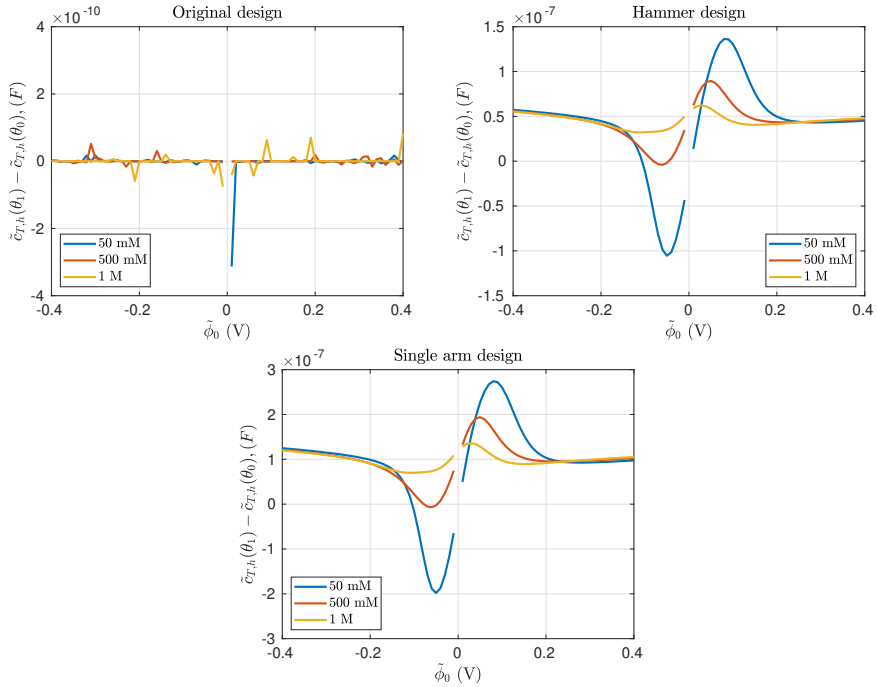


Figure 19. Representation of nanostructure shape signals over CV sweeps with varying ionic strength, which is given as molarity of NaCl in the legend.

Second, the hammer and single arm designs exhibit a significant odd-symmetric behavior in their signals, appearing within a small interval of applied voltage about $\tilde{\phi}_0 = 0$ V and magnified by low ionic strength. This is a critical feature of these DNA origami nanostructure shapes since biosensor test design may capitalize upon it. For instance, a test could measure the difference in capacitance with and without a given sample along voltages between the minimizer and maximizer of expected curves such as those shown in Figure 19, such that a positive test would produce a monotonically increasing curve and a negative test would show a horizontal line. Within this framework, denoising techniques employing isotonic regression can easily identify and exclude outlying measurements that do not follow the designed monotonicity [47]. Constrained optimization methodology can also be used to determine optimal salt concentrations, balancing the magnitude and slope of a positive test result with minimum concentrations of NaCl and $MgCl_2$ for nanostructure survival and maximum ion concentrations $\tilde{C}_i^{\max}$.

6. Conclusions

Biosensors are critical to providing accurate, rapid diagnostic measurements, significant for applications such as point-of-care medicine, food safety, and biosurveillence. Mathematical modeling of these devices is crucial as such research paves the way for device design improvement and uncertainty quantification of measurements. In pursuit of such investigations for the biosensor established in [11], this manuscript developed a novel model of transmuting DNA origami nanostructures and the surrounding electrochemical processes that constitute device signaling. A modified Poisson-Boltzmann equation described the behavior of the electric potential under an applied voltage, incorporating steric effects from ion crowding and the Born force. The nanostructure was represented as a variation in permittivity and an added background charge within two bounding polygons acting as the nanostructure's arms. Differential capacitance was used to calculate the system's capacitance from the model's variables. A finite difference method discretized the model, which was solved with an inexact Newton method. Capacitance was also approximated with finite differencing, as well as a Reimann sum to total values along the bottom surface.

Two nanostructure treatments, nonsmooth and smooth, were outlined and compared. In the approximation of the electric potential, the nonsmooth treatment was found to admit larger numerical error than the smooth treatment and lose an order of accuracy. This did not, however, entirely carry over to the capacitance approximation, where it was found that the smoothing length in the smooth nanostructure treatment likely causes differences in capacitance between the two treatments over the bulk of the tested applied voltages. Regardless, both nanostructure treatments produced capacitance curves of similar trend and magnitude, complicating a definitive suggestion of one treatment over the other.

With a parameter study, we investigated other potential influences on capacitance. Numerical error estimations suggested a minimum grid resolution and perturbation of applied voltage. Including auxiliary ions in our model as well as modifying maximum ion concentrations produced significant variations in the expected capacitance curves.

Preliminary observations in device sensitivity were then given, demonstrating that nanostructure stilt heights may decrease sensitivity if too high, and minimizing the length of the bottom arm of nanostructure designs may be advantageous. Special odd symmetry in the signal of the hammer and single arm designs was also shown, especially for cases with low ionic strength, motivating a biosensor test design capitalizing upon the observed monotonicity.

The work grounds further investigations into biosensor design improvement. The optimal shape and dimension of DNA origami nanostructures for signal amplification are especially anticipated, as these factors are expected to greatly influence signaling, but are strictly constrained by the number of DNA base pairs that constitute the structures. Ideal concentrations of NaCl and $MgCl_2$ for test design may also be investigated, as ionic strength was shown to influence the magnitude of the nanostructure's signal. Moreover, the simulation may aid in identifying confounding experimental factors, as well as in pursuits of measurement uncertainty quantification.

Use of AI tools declaration

The authors declare they have not used Artificial Intelligence (AI) tools in the creation of this article.

Disclaimer

This paper is an official contribution of the National Institute of Standards and Technology and is not subject to copyright in the United States. Commercial products are identified in order to adequately specify certain procedures. In no case does such identification imply recommendation or endorsement by the National Institute of Standards and Technology, nor does it imply that the identified products are necessarily the best available for the purpose.

Conflicts of interest

All authors declare no conflicts of interest in this paper.

Acknowledgments

The authors thank Arvind Balijepalli, Jacob Majikes, and Ruohong Shi for fruitful discussions and pointed modeling suggestions, as their knowledge was invaluable. The authors also thank the reviewers for their suggestions and opportunity to strengthen this work. This research was performed while A.M.C. held a National Institute of Standards and Technology (NIST) National Research Council (NRC) Research Postdoctoral Associateship Award at the NIST Applied and Computational Mathematics Division under the supervision of A.J.K.

References

1. M. T. Amen, T. T. T. Pham, E. Cheah, D. P. Tran, B. Thierry, Metal-oxide FET biosensor for point-of-care testing: Overview and perspective, *Molecules*, **27** (2022), 7952. https://doi.org/10.3390/molecules27227952
2. I. Nastasijevic, I. Kundacina, S. Jaric, Z. Pavlovic, M. Radovic, V. Radonic, Recent advances in biosensor technologies for meat production chain, *Foods*, **14** (2025), 744. https://doi.org/10.3390/foods14050744
3. Q. Wang, Z. A. Zhao, K. Y. Yao, Y. L. Cheng, D. S. H. Wong, D. W. C. Wong, et al., The versatility of biological field-effect transistor-based biosensors (BioFETs) in point-of-care diagnostics: Applications and future directions for peritoneal dialysis monitoring, *Biosensors*, **15** (2025), 193. https://doi.org/10.3390/bios15030193
4. B. M. Paddle, Biosensors for chemical and biological agents of defence interest, *Biosens. Bioelecton.*, **11** (1996), 1079–1113. https://doi.org/10.1016/0956-5663(96)82333-5
5. S. T. Le, S. Cho, C. A. Richter, A. Balijepalli, Optimal field-effect transistor operation for high-resolution biochemical measurements, *Rev. Sci. Instrum.*, **92** (2021), 030901. https://doi.org/10.1063/5.0025847
6. S. T. Le, S. Cho, A. Zaslavsky, C. A. Richter, A. Balijepalli, High-performance dual-gate graphene pH sensors, *Appl. Phys. Lett.*, **120** (2022), 263701. https://doi.org/10.1063/5.0086049
7. S. Cho, A. Zaslavsky, C. A. Richter, J. M. Majikes, J. A. Liddle, F. Andrieu, et al., High-resolution DNA binding kinetics measurements with double gate FD-SOI transistors, in *2022 International Electron Devices Meeting (IEDM)*, 2022. https://doi.org/10.1109/IEDM45625.2022.10019493

8. M. Pandey, M. Bhaiyya, P. Rewatkar, J. B. Zalke, N. P. Narkhede and H. Haick, Advanced materials for biological field-effect transistors (Bio-FETs) in precision healthcare and biosensing, *Adv. Healthc. Mater.*, **14** (2025). https://doi.org/10.1002/adhm.202500400
9. N. Shafi, J. S. Parmaar, A. Porwal, A. M. Bhat, C. Sahu, C. Periasamy, Gate all around junctionless dielectric modulated BioFET based hybrid biosensor, *Silicon*, **13** (2021), 2041–2052. https://doi.org/10.1007/s12633-020-00583-2
10. M. K. Anvarifard, A. A. Orouji, Design of a novel high-sensitive SOI-junctionless BioFET overcoming sensitivity degradation problems, *Sci. Rep.*, **14** (2024), 18395. https://doi.org/10.1038/s41598-024-69383-7
11. J. Majikes, S. Cho, T. E. Cleveland, J. A. Liddle, A. Balijepalli, Variable gain DNA origami charge amplifiers for biosensing, *Nanoscale*, **16** (2024), 20893–20902. https://doi.org/10.1039/d4nr02959c
12. P. W. K. Rothemund, Folding DNA to create nanoscale shapes and patterns, *Nature*, **440** (2006), 297–302. https://doi.org/10.1038/nature04586
13. M. S. Sajal, K. C. Lin, Y. Gilpin, V. Walawalkar, F. Dehghandehnavi, R. E. Taylor, et al., Towards CMOS capacitance sensors for DNA origami characterization, in *2023 International Electron Devices Meeting (IEDM)*, 2023. https://doi.org/10.1109/IEDM45741.2023.10413681
14. A. C. Stelson, M. Liu, C. A. E. Little, C. J. Long, N. D. Orloff, N. Stephanopoulos, et al., Label-free detection of conformational changes in switchable DNA nanostructures with microwave microfluidics, *Nat. Commun.*, **10** (2019), 1174. https://doi.org/10.1038/s41467-019-09017-z
15. F. Kroener, A. Heerwig, W. Kaiser, M. Mertig, U. Rant, Electrical actuation of a DNA origami nanolever on an electrode, *J. Am. Chem. Soc.*, **139** (2017), 16510–16513. https://doi.org/10.1021/jacs.7b10862
16. F. Kroener, L. Traxler, A. Heerwig, U. Rant, M. Mertig, Magnesium-dependent electrical actuation and stability of DNA origami rods, *Appl. Mater. Interfaces*, **11** (2018), 2295–2301. https://doi.org/10.1021/acsami.8b18611
17. N. Arroyo-Currás, M. Sadeia, A. K. Ng, Y. Fyodorova, N. Williams, T. Afif, et al., An electrochemical biosensor exploiting binding-induced changes in electron transfer of electrode-attached DNA origami to detect hundred nanometer-scale targets, *Nanoscale*, **12** (2020), 13907–13911. https://doi.org/10.1039/d0nr00952k
18. N. Smoliak, N. Kumar, P. M. Parreira, C. Macdonald, V. Georgiev, A hybrid analytical and machine learning model of BioFETs for the detection of peptides, *IEEE Sens. Lett.*, **9** (2025). https://doi.org/10.1109/LSENS.2025.3606612
19. S. Baumgartner, M. Vasicek, A. Bulyha, C. Heitzinger, Optimization of nanowire DNA sensor sensitivity using self-consistent simulation, *Nanotechnology*, **22** (2011). https://doi.org/10.1088/0957-4484/22/42/425503
20. C. Heitzinger, N. J. Mauser, C. Ringhofer, Multiscale modeling of planar and nanowire field-effect biosensors, *SIAM J. Appl. Math*, **70** (2010), 1634–1654. https://doi.org/10.1137/080725027

21. A. Bulyha, C. Heitzinger, An algorithm for three-dimensional Monte-Carlo simulation of charge distribution at biofunctionalized surfaces, *Nanoscale*, **3** (2011), 1608–1617. https://doi.org/10.1039/c0nr00791a
22. R. M. Evans, A. Balijepalli, A. J. Kearsley, Transport phenomena in biological field effect transistors, *SIAM J. Appl. Math.*, **80** (2020), 2586–2607. https://doi.org/10.1137/19M1255495
23. L. A. Melara, R. M. Evans, S. Cho, A. Balijepalli, A. J. Kearsley, Optimal bandwidth selection in stochastic regression of Bio-FET measurements, *J. Math. Biol.*, textbf91 (2025), 9. https://doi.org/10.1007/s00285-025-02231-y
24. G. Lin, Effects of multi-component small permanent charges on the dynamics of Poisson-Nernst-Planck models, *Math. Biosci. Eng.*, **23** (2026), 636–677. https://doi.org/10.3934/mbe.2026025
25. D. Tripathi, A. Yadav, O. A. Bég, Electro-kinetically driven peristaltic transport of viscoelastic physiological fluids through a finite length capillary: Mathematical modeling, *Math. Biosci.*, **283** (2017), 155–168. https://doi.org/10.1016/j.mbs.2016.11.017
26. J. Wu, Understanding the electric double-layer structure, capacitance, and charging dynamics, *Chem. Rev.*, **122** (2022), 10821–10859. https://doi.org/10.1021/acs.chemrev.2c00097
27. A. Ebrahimijahan, M. Abbaszadeh, M. Dehghan, Numerical solutions for the Poisson-Nernst-Planck system using integrated radial basis function and moving least squares techniques with reduced order method, *Eng. Comput.*, **41** (2025), 4757–4798. https://doi.org/10.1007/s00366-025-02198-w
28. N. Baker, M. Holst, F. Wang, Adaptive multilevel finite element solution of the Poisson-Boltzmann equation II. Refinement at solvent-accessible surfaces in biomolecular systems, *J. Comput. Chem.*, **21** (2004), 1343–1352. https://doi.org/10.1002/1096-987X(20001130)21:15<1343::AID-JCC2>3.0.CO;2-K
29. B. Lu, D. Zhang, J. A. McCammon, Computation of electrostatic forces between solvated molecules determined by the Poisson-Boltzmann equation using a boundary element method, *J. Chem. Phys.*, **122** (2005), 214102. https://doi.org/10.1063/1.1924448
30. M. Bosy, M. W. Scroggs, T. Betcke, E. Burman, C. D. Cooper, Coupling finite and boundary element methods to solve the Poisson–Boltzmann equation for electrostatics in molecular solvation, *J. Comput. Chem.*, **45** (2023), 787–797. https://doi.org/10.1002/jcc.27262
31. J. López-García, J. Horno, C. Grosse, Differential capacitance of the diffuse double layer at electrode-electrolyte interfaces considering ions as dielectric spheres: Part I. Binary electrolyte solutions, *J. Colloid Interface Sci.*, **496** (2017), 531–539. https://doi.org/10.1016/j.jcis.2017.02.043
32. M. Born, Volumen und hydratationswärme der ionen, *Z. Phys.*, **1** (1920), 45–48.
33. J. Bikerman, XXXIX. Structure and capacity of electrical double layer, *London, Edinburgh Dublin Philos. Mag. J. Sci.*, **33** (1942), 384–397. https://doi.org/10.1080/14786444208520813
34. B. J. Kirby, *Mirco- and Nanoscale Fluid Mechanics*, Cambridge University Press, New York, NY, 2010.
35. G. Valette, Double layer on silver single crystal electrodes in contact with electrolytes having anions which are slightly specifically adsorbed: Part II. The (100) face, *J. Electroanal. Chem. Interfacial Electrochem.*, **138** (1982), 37–54. https://doi.org/10.1016/0022-0728(82)87126-X

36. R. Sundararaman, K. Letchworth-Weaver, K. Schwarz, Improving accuracy of electrochemical capacitance and solvation energetics in first-principles calculations, *J. Chem. Phys.*, (2018), **148**. https://doi.org/10.1063/1.5024219

37. M. S. Shibata, Y. Morimoto, I. V. Zenyuk, A. Z. Weber, Parameter-fitting-free continuum modeling of electric double layer in aqueous electrolyte, *J. Chem. Theory Comput.*, **20** (2024), 6184–6196. https://doi.org/10.1021/acs.jctc.4c00408

38. X. Wang, K. Liu, J. Wu, Demystifying the Stern layer at a metal–electrolyte interface: Local dielectric constant, specific ion adsorption, and partial charge transfer, *J. Chem. Phys.*, **154** (2021), 124701. https://doi.org/10.1063/5.0043963

39. M. Y. Kiriukhin, K. D. Collins, Dynamic hydration numbers for biologically important ions, *Biophys. Chem.*, **99** (2002), 155–168. https://doi.org/10.1016/S0301-4622(02)00153-9

40. S. Wang, E. Alexov, S. Zhao, On regularization of charge singularities in solving the poisson-boltzmann equation with a smooth solute-solvent boundary, *Math. Biosci. Eng.*, **18** (2021), 1370–1405. https://doi.org/10.3934/mbe.2021072

41. A. Cuervo, P. D. Dans, J. L. Carrascosa, M. Orozco, G. Gomila, F. Laura, Direct measurement of the dielectric polarization properties of DNA, *Proc. Natl. Acad. Sci. U.S.A.*, **111** (2014), E3624–E3630. https://doi.org/10.1073/pnas.1405702111

42. J. Yoo, A. Aksimentiev, In situ structure and dynamics of DNA origami determined through molecular dynamics simulations, *Proc. Natl. Acad. Sci. U.S.A.*, **110** (2013), 20099–20104. https://doi.org/10.1073/pnas.1316521110

43. I. L. Chern, J. G. Liu, W. C. Wang, Accurate evaluation of electrostatics for macromolecules in solution, *Methods Appl. Anal.*, **10** (2003), 309–328.

44. Q. Cai, M. J. Hsieh, J. Wang, R. Luo, Performance of nonlinear finite-difference Poisson-Boltzmann solvers, *J. Chem. Theory Comput.*, **6** (2010), 203–211. https://doi.org/10.1021/ct900381r

45. L. Armijo, Minimization of functions having Lipschitz continuous first partial derivatives, *Pac. J. Math.*, **19** (1966), 1–3. https://doi.org/10.2140/pjm.1966.16.1

46. D. M. Kolb, J. Schneider, The study of reconstructed electrode surfaces: Au(100)-(5×20), *Surf. Sci.*, **162** (1985), 764–775. https://doi.org/10.1016/0039-6028(85)90977-X

47. A. J. Kearsely, Projections onto order simplexes and isotonic regression, *J. Res. Natl. Inst. Stand. Technol.*, **111** (2006), 121–125. https://doi.org/10.6028/jres.111.011

48. G. Leoni, *A First Course in Sobolev Spaces*, American Mathematical Society, Providence, Rhode Island, 2009.

49. B. Dacorogna, *Direct Methods in the Calculus of Variations*, 2nd edition, Springer, New York, NY, 2008. https://doi.org/10.1007/978-0-387-55249-1

50. Z. Huang, B. Li, Variational analysis of the classical and ionic size-modified Poisson–Boltzmann electrostatics, *SIAM J. Math. Anal.*, **58** (2026), 991–1016. https://doi.org/10.1137/25M1769314

51. B. Li, Continuum electrostatics for ionic solutions with non-uniform ionic sizes, *Nonlinearity*, **5228** (2009), 811–833. https://doi.org/10.1088/0951-7715/22/4/007

52. B. Li, Minimization of electrostatic free energy and the Poisson–Boltzmann equation for molecular solvation with implicit solvent, *SIAM J. Math. Anal.*, **40** (2009), 2536–2566. https://doi.org/10.1137/080712350

Appendix

A. Argument for differential capacitance

Here we demonstrate the applicability of differential capacitance (2.12) to our model. We work with the established nondimensional model (2.9), although it is apparent that the dimensional case follows. Define the energy $E\colon H^1(\Omega) \to \mathbb{R}$, where $H^1(\Omega)$ is the Sobolev space of order one [48], as

$$E(\phi) = \int_\Omega \left[\frac{\varepsilon(\mathbf{x})}{2} |\nabla \phi(\mathbf{x})|^2 + F(\mathbf{x}; \phi(\mathbf{x})) - P(\mathbf{x})\phi(\mathbf{x}) \right] \mathrm{d}\mathbf{x}. \tag{A.1}$$

Assuming sufficient regularity, the Euler-Lagrange equation [49] for (A.1) is

$$\nabla \cdot (\varepsilon \nabla \phi) = \frac{\partial F}{\partial \phi} - P, \tag{A.2}$$

such that taking F to satisfy

$$\frac{\partial F}{\partial \phi} = -\sum_{i=1}^{N_{ions}} z_i C_i(\phi), \tag{A.3}$$

returns the mPB equation (2.9). As a consequence, we may identify solutions to (A.2) by minimizing E among functions with boundary conditions (2.11). In particular, for the generalized boundary condition $\phi(x, 0) = \phi_0$, we may write the dimensional stationary energy as

$$\mathcal{E}(\phi_0) = \min \left\{ E(\phi) \,|\, \phi \in H^1(\Omega), \phi(x, 0) = \phi_0 \right\}. \tag{A.4}$$

Varying the applied voltage ϕ_0 causes charge, denoted Q, to be stored according to the relation

$$Q = \frac{\mathrm{d}\mathcal{E}}{\mathrm{d}\phi_0}. \tag{A.5}$$

Now suppose that a smooth family of minimizers $\phi^* = \phi^*(\phi_0)$ exists and is unique (conditions for this are shown in the subsequent appendix). Then, roughly, we may compute Q via the following:

$$\begin{aligned}
Q &= \frac{\mathrm{d}}{\mathrm{d}\phi_0} \left[E(\phi^*) \right] && \text{(A.6a)} \\
&= \int_\Omega \left[\varepsilon \nabla \phi^* \cdot \nabla \frac{\partial \phi^*}{\partial \phi_0} + \frac{\partial F}{\partial \phi^*} \frac{\partial \phi^*}{\partial \phi_0} - P \frac{\partial \phi^*}{\partial \phi_0} \right] \mathrm{d}\mathbf{x} && \text{(A.6b)} \\
&= \int_{\partial\Omega} \varepsilon \frac{\partial \phi^*}{\partial n} \frac{\partial \phi^*}{\partial \phi_0} \,\mathrm{d}S + \int_\Omega \left[-\nabla \cdot (\varepsilon \nabla \phi^*) + \frac{\partial F^*}{\partial \phi} - P \right] \frac{\partial \phi^*}{\partial \phi_0} \,\mathrm{d}\mathbf{x} && \text{(A.6c)} \\
&= \int_{\partial\Omega} \varepsilon \frac{\partial \phi^*}{\partial n} \,\mathrm{d}S, && \text{(A.6d)}
\end{aligned}$$

since $\frac{\partial \phi^*}{\partial \phi_0} = 1$ along $y = 0$, and the condition at $y \to \infty$ and periodicity in x makes zero contribution to the integral. Note that Q takes no direct contribution from the DNA origami nanostructure represented by variation in ε, P, as any such fluctuations exist sufficiently far from the boundary. Thus, the use of differential capacitance is supported within our model. For a more formal justification, care must be exercised to ensure $\frac{\partial \phi^*}{\partial \phi_0}$ is a valid test function dependent upon the regularity of E, although it can be seen that the result remains.

B. Existence and uniqueness of minimizers ϕ^*

This appendix derives a condition to ensure the existence and uniqueness of minimizers ϕ^* of the nondimensional energy functional (A.1) defined in Appendix A. One such existence and uniqueness theorem we could prove is the following.

Theorem 1. *Suppose $\varepsilon\colon \Omega \to [0, +\infty)$ is measurable and satisfies $\varepsilon_a < \varepsilon < \varepsilon_b$ for some $\varepsilon_a, \varepsilon_b > 0$; $P\colon \Omega \to \mathbb{R}$ is measurable, bounded, and compactly supported; and $F\colon \Omega \times \mathbb{R} \to \mathbb{R}$ is convex and C^2 in the second argument, and measurable in the first such that*

$$\frac{\partial F}{\partial \phi}(\mathbf{x}; \phi(\mathbf{x})) = -\sum_{i=1}^{N_{ions}} z_i C_i(\mathbf{x}; \phi(\mathbf{x})). \tag{B.1}$$

Then, the functional

$$E(\phi) = \int_\Omega \left[\frac{\varepsilon(\mathbf{x})}{2} |\nabla \phi(\mathbf{x})|^2 + F(\mathbf{x}; \phi(\mathbf{x})) - P(\mathbf{x})\phi(\mathbf{x}) \right] d\mathbf{x}, \tag{B.2}$$

admits a unique minimizer among $H^1(\Omega)$ functions with boundary condition (2.11) *which satisfies the mPB equation* (2.9) *in the weak sense of distributions.*

For brevity, we provide a quick overview of a proof by the direct method of the calculus of variations [49]. From the assumptions on ε and P, it may be seen that the functional E is weakly coercive in $H^1(\Omega)$. In particular, since Ω admits a Poincaré inequality [48, Theorem 12.17], we may show that E satisfies the inequality

$$E(\phi) \geq \alpha \|\phi\|^2_{H^1(\Omega)} - \beta, \tag{B.3}$$

for some $\alpha > 0, \beta \in \mathbb{R}$. Since convexity of E in $\nabla\phi$ is equivalent to weak lower-semicontinuity of E [49, Theorem 3.15 & Corollary 3.24], Theorem 1 combined with weak coercivity gives the existence of a minimizer on Ω. Uniqueness of the minimizer is a consequence of strict convexity of E, which itself is a consequence of strict convexity of the map $\phi \mapsto \frac{\varepsilon}{2}|\nabla\phi|^2$ and convexity of F in the second argument.

Convexity of the function F is nuanced and has been discussed before in the context of the modified Poisson-Boltzmann equation [50–52]. While we cannot give a sufficient condition that F is convex everywhere, the following proposition establishes that for sufficiently small ϕ, F is convex and therefore by Theorem 1, solutions to the mPB equation are unique.

Proposition 1. *Let $F \in C^2(\mathbb{R})$ be a function satisfying* (A.3) *and the dilute charge balance condition*

$$\sum_{i=1}^{N_{ions}} z_i C_i^{\infty} = 0. \tag{B.4}$$

Then, F is strictly convex in a neighborhood of $\phi = 0$.

Proof. Since $F \in C^2(\mathbb{R})$, it may be shown that F is strictly convex by verifying

$$\frac{\partial^2 F}{\partial \phi^2} > 0. \tag{B.5}$$

From (A.3) and (2.10), we find

$$\frac{\partial^2 F}{\partial \phi^2} = -\sum_{i=1}^{N_{ions}} z_i \frac{\partial C_i}{\partial \phi} \tag{B.6a}$$

$$= -\sum_{i=1}^{N_{ions}} z_i \left(\frac{-z_i \nu C_i^{\infty} e^{B_i(1/\varepsilon_w - 1/\varepsilon)} e^{-z_i \nu \phi}}{1 + \sum_{\iota=1}^{N_{ions}} \frac{C_\iota^{\infty}}{C_\iota^{\max}} (e^{B_\iota(1/\varepsilon_w - 1/\varepsilon)} e^{-z_\iota \nu \phi} - 1)} \right. \tag{B.6b}$$

$$\left. + \frac{\nu C_i^{\infty} \sum_{\iota=1}^{N_{ions}} \frac{C_\iota^{\infty}}{C_\iota^{\max}} z_\iota e^{(B_i + B_\iota)(1/\varepsilon_w - 1/\varepsilon)} e^{-(z_i + z_\iota)\nu\phi}}{\left(1 + \sum_{\iota=1}^{N_{ions}} \frac{C_\iota^{\infty}}{C_\iota^{\max}} (e^{B_\iota(1/\varepsilon_w - 1/\varepsilon)} e^{-z_\iota \nu \phi} - 1)\right)^2} \right) \tag{B.6c}$$

$$= \sum_{i=1}^{N_{ions}} z_i^2 \nu C_i(\phi) - \left(\sum_{i=1}^{N_{ions}} z_i C_i(\phi) \right) \left(\sum_{\iota=1}^{N_{ions}} z_\iota \nu \frac{C_\iota(\phi)}{C_\iota^{max}} \right). \tag{B.6d}$$

The first term in (B.6d) is strictly positive since $C_i(\phi) > 0$. Furthermore, by the charge balance condition (B.4), we have that

$$\sum_{i=1}^{N_{ions}} z_i C_i(0) = \sum_{i=1}^{N_{ions}} z_i C_i^{\infty} = 0,$$

so $\frac{\partial^2 F}{\partial \phi^2} > 0$ at $\phi = 0$. Therefore, by continuity of $\frac{\partial^2 F}{\partial \phi^2}$, we must have that it is positive in a neighborhood of $\phi = 0$. Therefore, F is strictly convex in this neighborhood. □

AIMS Press

© 2026 the Author(s), licensee AIMS Press. This is an open access article distributed under the terms of the Creative Commons Attribution License (http://creativecommons.org/licenses/by/4.0)